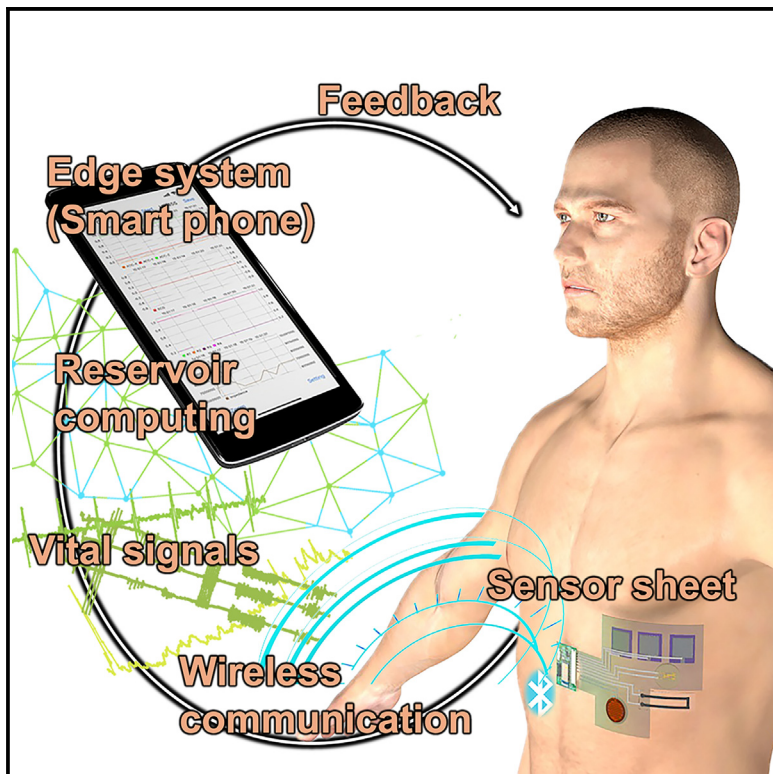


Real-time personal healthcare data analysis using edge computing for multimodal wearable sensors

Graphical abstract



Authors

Guren Matsumura, Satoko Honda,
Takamasa Kikuchi, ..., Kiyoshi Hayakawa,
Kohei Nakajima, Kuniharu Takei

Correspondence

k-nakajima@isi.imi.i.u-tokyo.ac.jp (K.N.),
takei@ist.hokudai.ac.jp (K.T.)

In brief

We present an edge-type multimodal sensor patch for remote healthcare applications. The system uses multiple flexible sensors and a reservoir computing algorithm. As a fully functional and independent system, the sensor patch is integrated with a smartphone app enabled by the reservoir computing algorithm. As a demonstration, we showcase the multimodal sensor patch for detecting some vital conditions as an edge system.

Highlights

- Multimodal sensor patch allowing for continuous monitoring of vital signals
- Real-time personal healthcare data analysis
- Optimal reservoir computing algorithm with high generalization
- Demonstrated edge system for real-time monitoring



Validate

Functional device with real-world testing,
ready to scale

Matsumura et al., 2025, Device 3, 100597
February 21, 2025 © 2024 The Author(s).
Published by Elsevier Inc.
<https://doi.org/10.1016/j.device.2024.100597>

Article

Real-time personal healthcare data analysis using edge computing for multimodal wearable sensors

Guren Matsumura,¹ Satoko Honda,¹ Takamasa Kikuchi,² Yuuki Mizuno,² Hyuga Hara,¹ Yoshiki Kondo,³ Haruki Nakamura,^{1,3} Shin Watanabe,⁴ Kiyoshi Hayakawa,² Kohei Nakajima,^{5,*} and Kuniharu Takei^{3,6,*}

¹Department of Physics and Electronics, Osaka Metropolitan University, Sakai, Osaka 599-8531, Japan

²Industrial Systems Engineering of Intelligent Informatics Course, Osaka Metropolitan University College of Technology, Neyagawa, Osaka 572-8572, Japan

³Graduate School of Information Science and Technology, Hokkaido University, Sapporo, Hokkaido 060-0814, Japan

⁴Department of Emergency and Disaster Medicine, Juntendo University, Tokyo 113-8656, Japan

⁵Graduate School of Information Science and Technology, University of Tokyo, Tokyo 113-8656, Japan

⁶Lead contact

*Correspondence: k-nakajima@isi.imi.i.u-tokyo.ac.jp (K.N.), takei@ist.hokudai.ac.jp (K.T.)

<https://doi.org/10.1016/j.device.2024.100597>

THE BIGGER PICTURE To improve the applicability of personal health and fitness tracking devices, sensor or multi-sensor systems need to collect and analyze diverse signals (e.g., skin temperature, heart rate, breathing volume and frequency, etc.) as quickly as possible with as little computing and as few power resources as possible. This system-level development faces difficulties in hardware and software integrations, which involve interdisciplinary research such as device physics, machine learning, and system development. Here, we present a multimodal healthcare sensor patch system monitoring multiple vital signals in real time, including skin temperature, electrocardiogram, respiration, skin humidity, and activity. Because of the edge-computing system design (i.e., without the need to offload data processing to a centralized server), the data processing is done using a smartphone, which analyzes and presents the signals measured by the sensor patch without the need for a cloud or internet connection.

SUMMARY

Wireless, multimodal, wearable sensor patches can perform remote diagnosis and monitoring. By integrating multiple sensors, multimodal, wearable patches generate large datasets. Complex data correlation and analyses of large datasets for real-time, automatic edge-type systems are challenging. Here, we present an integrated wearable sensor patch with edge computing for remote healthcare applications powered by reservoir computing. This sensor patch system is integrated with flexible sensors for electrocardiography, respiration, skin temperature, and skin humidity. Vital and activity data can be applied to monitor coughing, arrhythmias, and posture using a machine learning algorithm. Importantly, all measurements, wireless data transmission, and real-time data analyses are processed in a smartphone as an edge-computing system, which allows quick, real-time feedback to users without using a cloud network system.

INTRODUCTION

Wearable devices can monitor vital signals continuously and automatically.¹ To improve the adhesion of these devices to skin, bandage-like sensors have been designed to monitor cardiac activity,^{2–5} skin temperature,^{6,7} respiration,^{8–11} chemical substances in sweat,^{12–18} and perspiration rate.^{19–21} For wearable personal healthcare monitoring, real-time data analyses from large amounts of continuous vital data are important. For real-time monitoring, reservoir computing (RC), which is a recur-

rent neural network, allows for fast data analyses without using high-performance computers resulting in the realization of an edge system.²² The edge system can help alleviate the processing power requirement for analyzing large datasets of these multimodal and integrated sensors for real-time feedback. For practical applications, the edge-computing system design must consider the hardware integration of different sensors and the software to translate the multimodal readouts to meaningful data about vital signs and the power and time efficiency to provide real-time feedback. While many studies tend to focus on



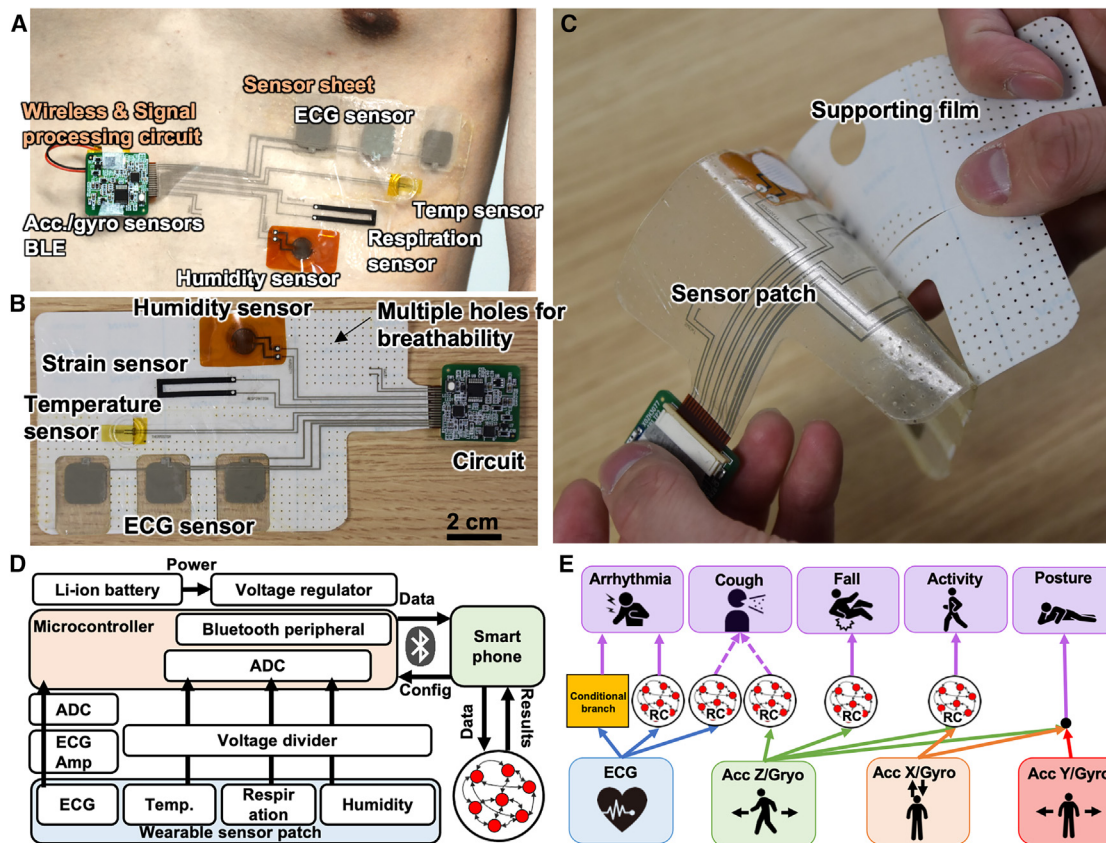


Figure 1. An edge-computing, wearable sensor patch and sensor characteristics

- (A) Photo of a wearable sensor patch.
- (B) Photos of the multimodal flexible sensor patch with the supporting film.
- (C) Photo of the sensor patch during delaminating the supporting film.
- (D) Detailed system diagram.
- (E) Machine learning algorithm.

improving the hardware performance and versatility of different sensors, there is a need for more efficient software design incorporated with multimodal flexible sensors for analyzing multiple vital parameters and providing real-time feedback to users, such as the use of edge computing.²³

We present a multimodal flexible sensor patch that uses edge computing to measure and analyze multiple vital signals and provide real-time feedback via a smartphone app. The device integrates multimodal flexible sensors, real-time machine learning data analyses, and remote vital monitoring using a smartphone as an edge system. The sensor patch uses a flexible film that can adhere to human skin (Figure 1A). The detailed structure and fabrication process are explained in the supplemental information (Figure S1), and the designed components are described in Figure S2. The multimodal, flexible sensor patch can monitor cardiac activity via electrocardiogram (ECG), respiration, skin temperature, and humidity caused by perspiration. A data processing circuit and a Bluetooth Low-Energy (BLE) module on a printed circuit board are connected to the flexible sensor patch for wireless data transmission. An accelerometer (ACC) is also installed to monitor physical activity and posture. The complete

device is shown in Figures 1B and 1C. After processing analog-to-digital conversion and transmitting the signals to the smartphone via BLE (Figure 1D), the datasets are analyzed to identify abnormalities such as arrhythmias, coughs, and falls in real time. For these real-time data analyses, a machine learning algorithm using RC²² is developed (see Figure 1E) and incorporated with the smartphone app. The main data analyses are conducted by an optimal RC algorithm installed in the smartphone as the edge computing.

RESULTS AND DISCUSSION

Long-term stable characteristics of multimodal flexible sensor

A flexible temperature sensor, humidity sensor, and strain sensors were integrated to monitor skin temperature, skin humidity, and respiration, respectively. These are all resistive-type sensors. To confirm long-term stability for daily use, sensor output characteristics at different temperatures and humidities were investigated. First, each sensor response to each stimulus was characterized using the resistance change ratio, $\Delta R/R_0$, where

R_0 is the initial resistance at room temperature, relative humidity (RH), and relaxed state of strain for each sensor. ΔR is the resistance change from R_0 at measured conditions. A temperature sensor fabricated by Au electrodes shows a resistance increase at higher temperatures, suggesting a positive thermal coefficient caused by thermal scattering of electrons in the Au electrode (Figure 2A). Using linear fitting of the results, the sensitivity was found to be $\sim 0.12\%/\text{ }^\circ\text{C}$. A humidity sensor consisting of stacked ZnIn₂S₄ (ZIS) nanosheets was integrated into this film. Resistance decreases when RH increases due to proton hopping on the surface of ZIS²⁴ (Figure 2B). The characterization of the humidity sensor was conducted at $34\text{ }^\circ\text{C}$ while the RH changed. The resistance change ratio when RH changed was relatively large ($>1\%/\%$, which is the resistance change ratio per RH); however, there are two step trends, depending on the humidity level, such that the specific sensitivity cannot be defined. The strain sensor was fabricated using conductive, laser-induced graphene (LIG) embedded in polydimethylsiloxane (PDMS). Resistance increases by a relatively large value ($>4\%/\%$, which is the resistance change ratio per strain) with increasing tensile strain in the film because LIG is physically stretched and the electrical path increases (Figure 2C). In addition, contacts between LIGs are also changed due to the porous structure of the LIG film. The gauge factor (GF), calculated from $\Delta R/R_0/\text{strain}$, was extracted by linear fitting from the forward data shown in Figure 2C. The GF was ~ 5.7 (coefficient of determination $r^2 = 1$) below 6.8% strain and ~ 15.0 ($r^2 = 0.9999$) between 6.8% and 13.3% strain. Importantly, the hysteresis of LIG/PDMS is small when strain is applied and released. Although the detection limits of each sensor were not measured in this study, the sensors had enough sensing capability to be used for the wearable application.

The mechanical properties of each sensor were characterized by bending the sensors physically. For the temperature sensor (Figure 2D), the maximum resistance change ratio from the flat state was $\sim 0.27\%$, the fluctuation of which is relatively large due to strain in the sensor. To suppress this bending effect, a PDMS cap layer with an air chamber was attached to the temperature sensor, resulting in the temperature sensor hardly bending under the attachment of the sensor on a body. Furthermore, this PDMS cup layer with an air chamber, where the thermal conductivity of air ($\sim 0.024 \text{ W/m K}$) is much lower than PDMS ($\sim 0.14 \text{ W/m K}$), works to suppress the temperature change caused by environment change, resulting in stable skin temperature monitoring without affecting any environment temperature change being realized.⁷ For the humidity sensor, resistance change was observed by bending the sensor film (Figure 2E). Since there is no protection layer to suppress strain, relatively large strain is applied to the ZIS film by bending the sensor film. To achieve a stable humidity response, a moisture path filter was laminated on top of the humidity sensor. This filter suppresses physical bending because the sensor with the filter is mechanically stiffer than the other region. Additionally, the filter prevents sweat from coming into direct contact with the sensor, ensuring stable humidity detection. For the strain sensor, decreasing the bending radius increases the resistance (Figure 2F), which is consistent with the results under stretching (Figure 2C), because the strain is inversely proportional to the radii.

The response time of each sensor was then measured to understand the sensor performance (Figure S3). Temperature and humidity sensors were tested by contacting a finger to the surface of the sensors. Due to the PDMS cap layer with the air chamber, the thermal response is relatively slow: about 20 s for response and 260 s for recovery times (Figure S3A). Although this cap layer has slower responses, it is beneficial to have this cap layer to measure skin temperature precisely without having large effects of environmental temperature change, and the response speed is within reason for the purpose of skin temperature monitoring. For the humidity sensor, response time is relatively fast (~ 0.04 s), while recovery time is slow, at ~ 14 s (Figure S3B). Similar to the temperature sensor, this slow response is acceptable for skin humidity monitoring due to the slow change of skin humidity. The strain sensor shows fast response and recovery times within ~ 0.2 s; however, the sensor output gradually decreases under tensile strain application and takes time to stabilize (Figure S3C). Since this strain sensor is used for peak-to-peak monitoring of resistance change caused by abdominal change corresponding to respiration, this output drift does not cause severe errors of the monitor respiration rate.

The integrated sensor sheet was tested for continuous monitoring under different temperatures and humidities (Figures 2G and 2H). While the strain sensor does not show any response to humidity changes, it exhibits a small temperature response of the strain sensor resistance with a sensitivity $\sim 0.79\%/\text{ }^\circ\text{C}$ (Figure 2I). There are two possible reasons for this: one is the thermal response of LIG itself and the other is thermal expansion of the LIG/PDMS film, resulting in resistance increases at high temperatures. Despite this slight sensitivity to temperature, the resistance change is much smaller than that of the strain response; thus, it can essentially be ignored for strain monitoring. Furthermore, because peaks of resistance change of the strain sensor every few seconds are used to calculate respiration rate, gradual temperature change does not affect respiration monitoring. Temperature and humidity sensors detected only temperature and humidity changes, respectively, with high selectivity (Figures 2J and 2K). As discussed in Figures 2D–2F, each sensor has a strain response by bending the sensor. To prevent this error caused by bending, the temperature sensor and the humidity sensor were covered by a three-dimensional air cap formed by PDMS and a water-proof filter, respectively, which are mechanically harder than the polyethylene terephthalate (PET) film. As the results show, each signal can be monitored precisely even during body motion because mechanical strain in the sensor during body motion is prevented. Importantly, all three sensors were relatively stable for more than 10 h of continuous monitoring. A commercially available gel sheet was used to monitor ECG signals from skin, and this ECG sensor was used for >10 h continuously.

To measure the breathability, the water vapor transmission rate (WVTR) was measured for the sensor patch (Figure S4). The WVTR for the sensor patch designed with holes was $\sim 97.8 \text{ g/m}^2/\text{h}$, which was 3 times higher than that of the PET film without holes. Each sensor performance was compared to other existing works (Table S1). Although the sensors do not have high sensitivity compared to others, the sensors show high stability for long-term measurements. More

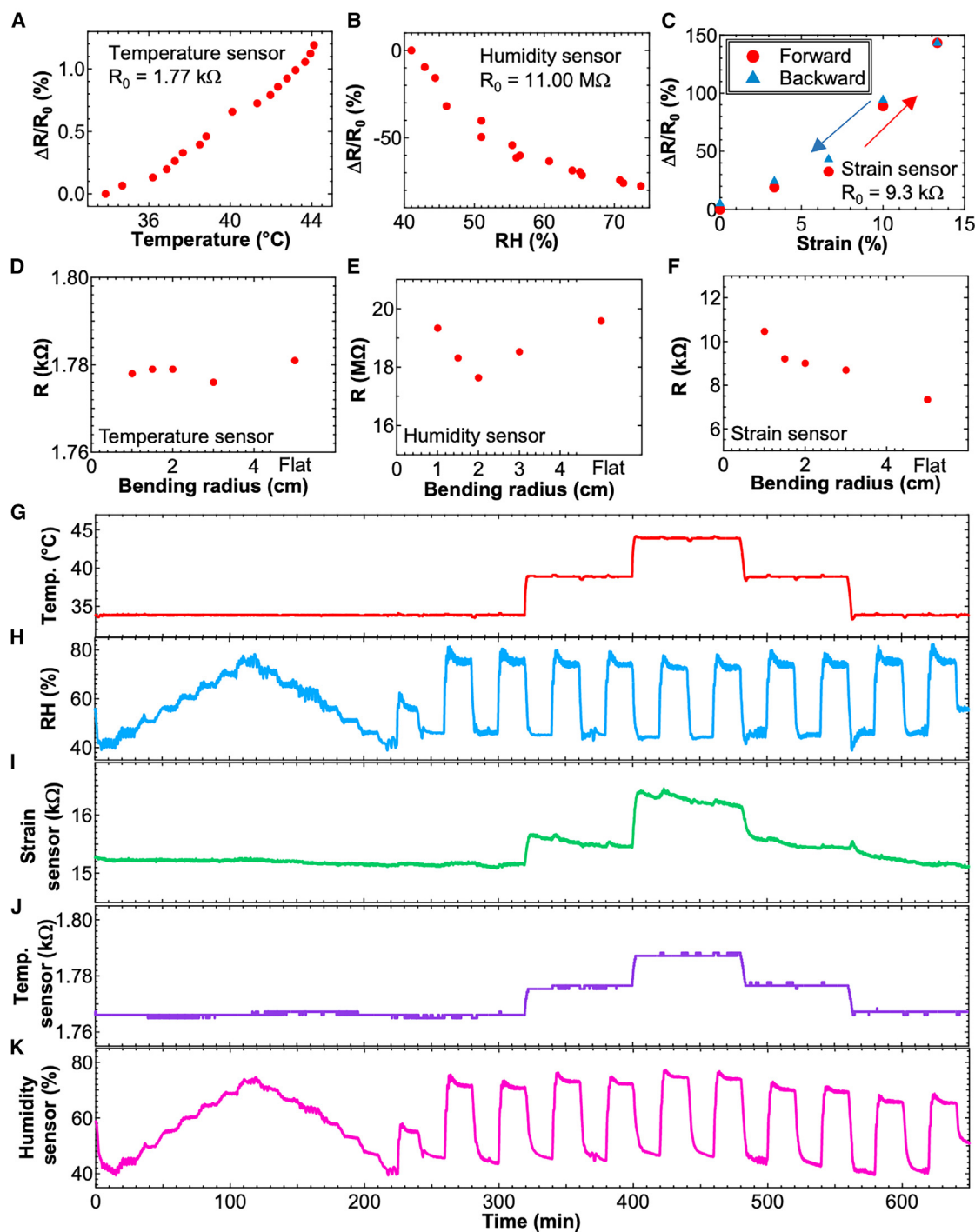


Figure 2. Sensor characteristics

(A–C) The resistance change ratio as a fundamental property of the (A) temperature sensor, (B) humidity sensor, and (C) strain sensor.

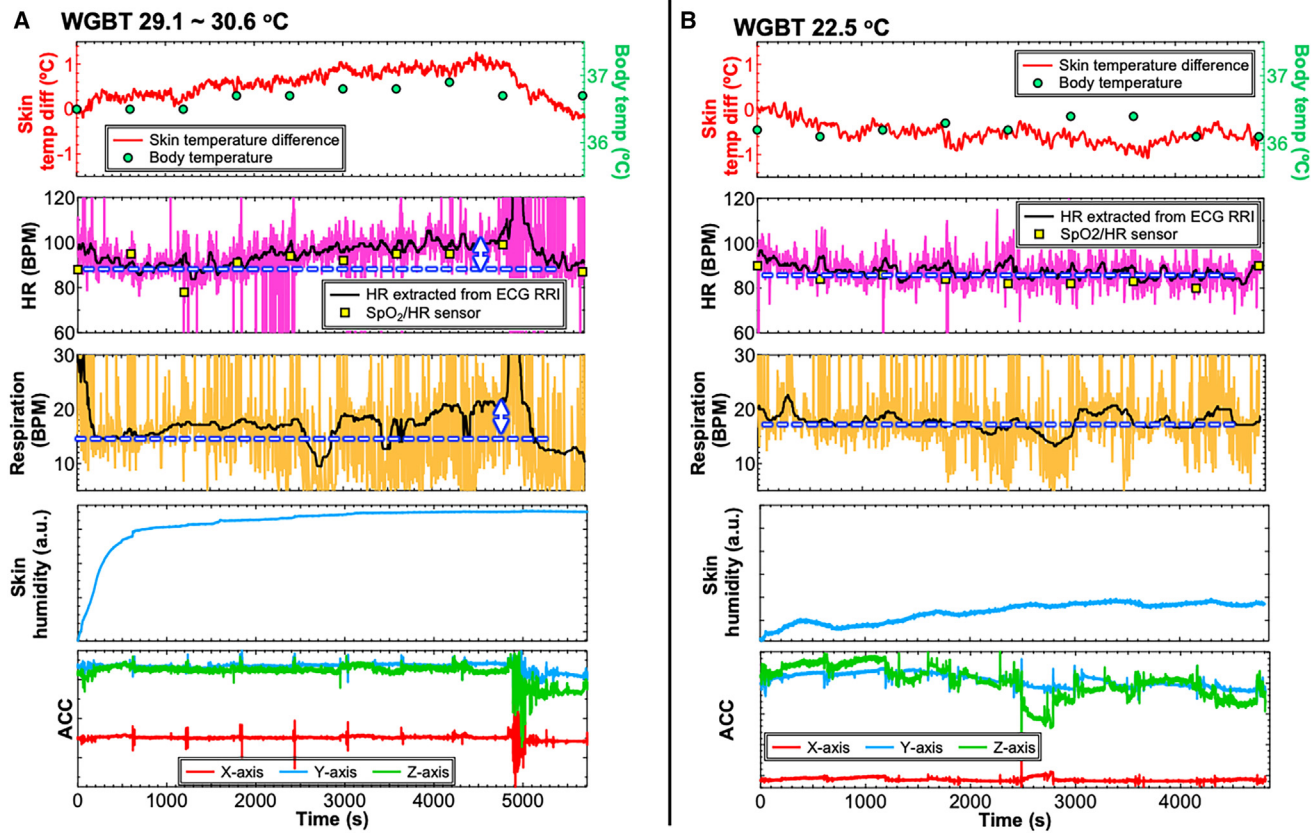
(D–F) Mechanical bending test of the (D) temperature sensor, (E) humidity sensor, and (F) strain sensor.

(G–K) Continuous sensor output monitoring in an environmental oven during (I) strain sensor, (J) temperature sensor, and (K) humidity sensor.

importantly, this study realized a flexible sensor integration with wireless monitoring for real-time vital multiple vital monitoring simultaneously.

Multiple vital monitoring

We tested the device on 3 volunteers (2 males and 1 females). Each volunteer wore the sensor patches on their chest in two

**Figure 3. Multimodal vital monitoring**

(and B) Real-time vital monitoring measured from volunteer #1 at (A) $\sim 30^\circ\text{C}$ and (B) 22.5°C . From top to bottom: skin temperature, heart rate, respiration rate, skin humidity, and ACC.

separate tests. The wearers first sat outside for 90 min in the direct sun with wet bulb globe temperatures (WBGT) between 29.1°C and 30.4°C , and second test was conducted in an air-conditioned room between $\sim 21.3^\circ\text{C}$ and 23.1°C . Figures 3, S5, and S6 display the real-time results. To compare the trends of skin and body temperature changes, a commercial body temperature sensor measured from the armpit was used. The measured skin temperature showed a similar trend to that of body temperature despite the larger variation (Figure S7A). This suggests that skin temperature may be used to monitor the trend of body temperature changes, after further data analyses and algorithm development.

The heart rate (HR) and respiration rate were extracted from R-R intervals (RRIs) of the ECG sensor and peak detection of strain sensor outputs, respectively (Figures 3, S5, and S6). (Here, R stands for R wave, which is a specific feature found in the ECG signal.) The HR extracted from RRIs of ECG, measured by a flexible ECG sensor, matched the output of an SpO₂ sensor monitored on a finger with a correlation coefficient of ~ 0.92 (Figure S7B). Humidity change was measured by the humidity sensor to monitor sweating. Note that the signal output was not converted to absolute humidity due to the difficulty of calibrating across batch-to-batch sensor variations. For the present purposes, the humidity change is more important than the abso-

lute value of skin moisture, and results without calibration did not affect the conclusions or concept of this study. Finally, an ACC was used to monitor activity. When the volunteer moved from outside to an air-conditioned room, the ECG signal had a lot of noises, and the strain sensor for respiration monitoring included signals resulting from body movements. These noises can be seen in the HR and respiration data around $\sim 5,000$ s in Figure 3A.

Participants diverged from either of two trends at $>29^\circ\text{C}$. Two of the volunteers exhibited some changes of their vitals under heat compared to the results at $\sim 23^\circ\text{C}$ (Figures 3 and S5), whereas the other one did not (Figure S6), possibly due to physiological differences. Although further medical trials to analyze these vital signal changes are required, this real-time, continuous vital change monitoring may have high potential to detect early-stage heat stress remotely. It should be noted that during these experiments, none of the volunteers displayed skin irritation from the sensor patch.

Real-time data analyses using an ESN

Here, we discuss the design of an echo state network (ESN),^{25,26} which is the type of RC framework we used for analyzing the data from our multimodal sensors. An ESN consists of mainly three layers: input, internal, and output. An ESN tunes only the output layer to obtain results, not the input or internal layer, and is

therefore relatively straightforward to implement on a smartphone as an edge system, and good accuracy can be obtained with short-time training. Details of the ESN used in this study are described in the [experimental procedures](#). An ESN with logistic regression in the output layer was employed to classify positive and negative states for the detection of arrhythmias, coughs, falls, and activity ([Figure 1E](#)). Ventricular extrasystolic beats were detected as an indicator for arrhythmia in this study. Conditional branches in addition to the ESN were used to analyze the signal from the ECG sensor to detect arrhythmia. For cough detection, data analyses of noise caused in ECG and output signals of ACC were employed. Activity detection was set to distinguish large movements, such as jumping, bending, walking, falling, and postural changes from standing up to sitting and lying down, using the sensor outputs of two axis (i.e., x and y) of ACC. In addition, a softmax function was used to assess ACC sensor outputs to classify standing and lying while facing up, right, left, and down.

To realize these tasks, other tests were conducted to collect further datasets, such as different postures, different activities, cough, and arrhythmia. All training and test data were collected following the action tasks described in [Table S2](#). One representative result involving a fall is shown in [Figures 4A–4C](#). Another dataset with arrhythmia signals is presented in [Figure S8](#). In addition to normal vital signals, when a subject coughed, noise signals in the ECG were observed ([Figure 4D](#)). Using these normal and abnormal signals, algorithms were developed to analyze all data. Training data ([Figure S9](#)) were generated from one subject who fell and seven subjects who did not. Using these data, a grid search for hyperparameters of the number of computational nodes (i.e., reservoir nodes), input scaling, spectral radius, and leaking rate was conducted in the ESN to achieve the best accuracy, where it is defined as

$$\text{accuracy}^* = \frac{\text{TP}^*}{\text{TP}^* + \text{FP}^* + \text{FN}^*},$$

where TP^* is the number of truly positive, FN^* is the number of falsely negative, and FP^* is the number of falsely positive signals for more than 1-step data with intervals defined in this study. This interval is a period during which the target signal turns from positive to negative. After 200 data steps of obtaining TP^* or FP^* signals, the prediction process stops to prevent simultaneous classification mistakes of both TP^* and FP^* signals. The optimized hyperparameters are shown in [Table S3](#). After the grid search of hyperparameters, an $\text{accuracy}^* = 1.0$ was obtained for fall detection ([Figure S10](#)).

Using the training data from two subjects with arrhythmias (28 arrhythmia signals in total) and the test data from nine subjects with and without arrhythmias ([Figure S11](#)), the accuracy^* was found to be 0.086. This low accuracy was due to the noise of ECG signals caused by body movement. To improve arrhythmia detection accuracy, Gaussian noise was added to the ECG signal training dataset as data augmentation to remove noise caused by body motion and coughing, resulting in the accuracy improving to 0.286 ([Figure S12](#)). However, accuracy was low using only raw ECG data and an ESN. This is because arrhythmia has two types of signals: abnormality in the amplitude and wave-

form and abnormality in the rhythm while the waveform remains normal. It is relatively easy to distinguish the abnormal waveform of ECG using a small number of nodes, but larger numbers of nodes are required to recognize the abnormal timing. However, a large number of nodes would decrease the calculation speed and increase power consumption. Because of this, we applied conditional branches without an ESN to help with the detection of abnormal timing, improving the accuracy^* to 0.931 (a detailed explanation is provided in the [experimental procedures](#)). When both the ESN and conditional branch analyses were integrated, accuracy^* improved to 0.966.

For cough detection, the training data ([Figure S13](#)) from two subjects and the test data from seven subjects (145 coughs) were used. To improve the accuracy^* of cough detection, ECG and z axis acceleration sensor outputs were applied. After optimization of the hyperparameter ([Figure S14; Note S1](#)), the accuracy^* reached 0.825. The system often incorrectly detected motion as a cough when subjects changed posture. To prevent such errors, when cough detection was positive and there was a posture change within 1.2 s of a cough, a data processing was introduced to remove artifacts caused by motion. This resulted in an $\text{accuracy}^* = 0.843$ ([Figure S15](#)). The strain sensor for respiration monitoring was not used for cough detection, although the sensor showed signal differences. This is because the amplitudes of strain sensor responses depend on the location of the sensor patch attached to volunteers, and the sensor itself has a small hysteresis ([Figure 2C](#)). This affects the results of accuracy and generalization. To obtain stable and consistent analyzed results, the strain sensor was not used for cough detection. The accuracy^* of cough detection was slightly low, 0.843. Because physiological data between subjects always differ, higher accuracy is difficult to realize with this learning method. However since an ESN is used in this system, training data can be updated during device use to optimize data analysis for better accuracy.

For activity detection, $F_{\beta\alpha}$, which is a weighted harmonic average of recall and precision, was used to evaluate outputs because accuracy cannot be properly evaluated due to the large number of negative states compared to positive states. $F_{\beta\alpha}$ is expressed by the following equation:

$$F_{\beta\alpha} = \frac{\frac{1+\beta^2}{1+\beta^2}}{\frac{\beta^2}{\text{precision}} + \frac{1}{\text{recall}}},$$

in which $\text{precision} = \text{TP}/(\text{TP} + \text{FP})$ and $\text{recall} = \text{TP}/(\text{TP} + \text{FN})$. $\beta = 0.5$ was set to create an evaluation index that emphasizes precision. With this definition, the training data from one subject ([Figure S16](#)), and the test data from seven subjects, $F_{\beta\alpha}$ was found to be 0.964 ([Figure S17](#)). All compiled results are summarized in [Figure 4E](#), and comparisons of different analyses using possible data processing are shown in [Figure 4F](#). In posture detection, high recall >0.97 for every posture was achieved ([Figure 4G](#)) using the training data ([Figure S18](#)) from two subjects and the test data from seven subjects. Activity detection with an ESN shows only a 0.051 improvement from that without an ESN. However, without an ESN, the threshold of the outputs from the ACC needs to be set depending on the user to determine the activity

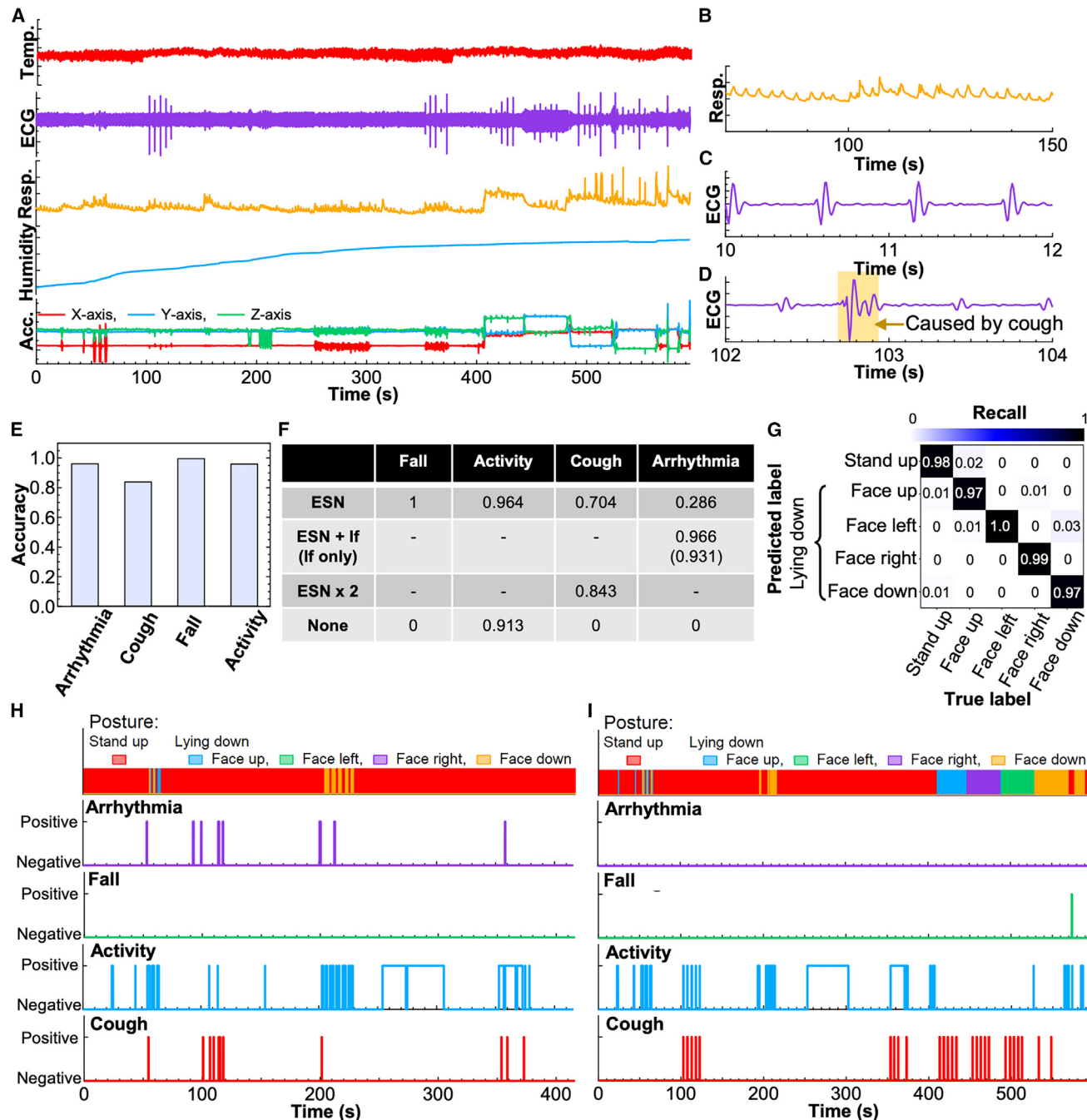


Figure 4. ESN analyses

(A) All sensor outputs in real time during different actions.

(B–D) Enlarged vital signals of (B) respiration, (C) ECG, and (D) ECG with noise caused by a cough.

(E) Accuracy of arrhythmia, cough, fall, and activity predictions.

(F) Comparisons of accuracy using algorithms with/without ESN and conditional branch.

(G) Confusion matrix of postures.

(H and I) Continuous vital data analyses using the prediction systems with (H) arrhythmia outputs and (I) fall output.

accurately. For the edge system, generalization that does not depend on the users is an important factor, which is something the ESN can provide.

The accuracy and calculation speed are also evaluated for arrhythmia and activity detections. For the performance comparison, the calculation speed was measured with an

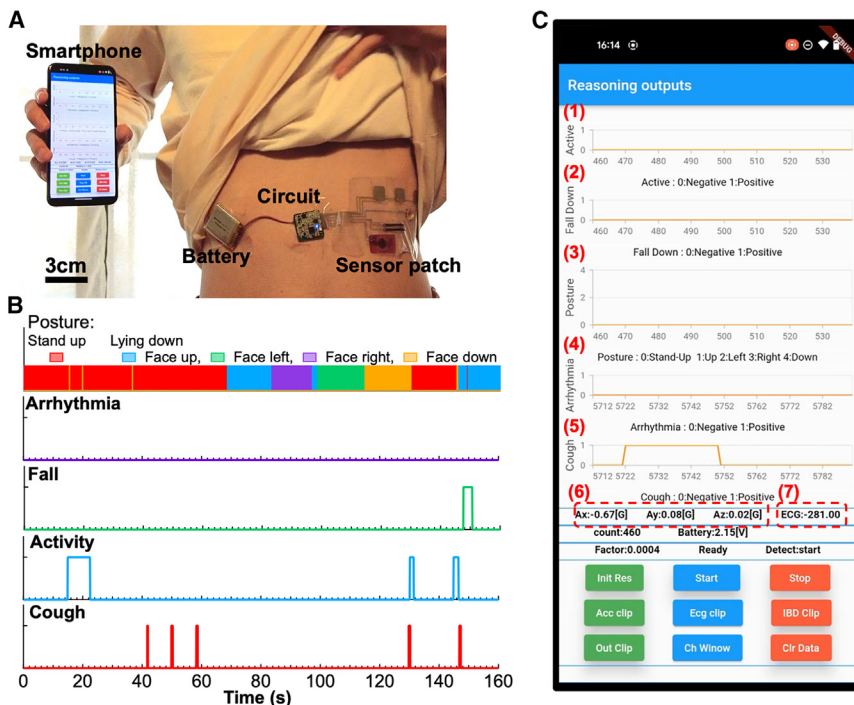


Figure 5. Edge-computing wearable sensor demonstration

(A) Photo of an installed machine learning smartphone app and wearable sensor patch on a subject.

(B) Real-time results analyzed by smartphone.

(C) Display of real-time edge-computing smartphone. The display shows (1) activity, (2) fall, (3) posture, (4) arrhythmia, (5) cough, (6) Ax, x axis; Ay, y axis; and Az, z axis of acceleration sensor, and (7) ECG amplitude from top.

were integrated on a disposable patch, and each sensor achieves sufficient stability for use in vital recording from skin. With this sensor patch, vital data were collected at both $>29^{\circ}\text{C}$ and $\sim 22^{\circ}\text{C}$ for early-stage heat stress detection. Although further study is required to define a threshold for symptoms of heat stress in the earliest stage, clear vital changes with time at $>29^{\circ}\text{C}$ were recorded, demonstrating that this system could potentially be used for heat stress detection. After confirming that the sensor patch can

detect stable vital data from skin, output signals were analyzed using an ESN to evaluate data automatically and detect other symptoms such as coughs, arrhythmias, and falls. Although physiological data often differ between subjects, a high accuracy of predictions $>80\%$ was achieved. Finally, the ESN algorithm was installed in a smartphone as an edge-computing system, and signal analyses were accomplished in the smartphone without using the internet. This multimodal sensor patch allows for the detection of multiple vital signals simultaneously. However, this edge system can only utilize the output signals of ECG and ACC to analyze the conditions. To utilize full datasets including respiration rate, skin temperature, and skin humidity, clinical trials comparing the commercial medical tools must be conducted to find early-stage symptoms of disease.

To improve output using the owner's vital data, a training process on an edge system is ideal. It is possible to augment training data with user data, due to the use of an ESN, with low computational power and a simple computation process. In fact, it took less than 30 min to train all detection items for the use of the ESN on a laptop computer. Simplifying some additional data processing, such as data augmentation for further training, will enable quick incorporation of this training process in a smartphone. Although there are still challenges as mentioned above, this edge-computing, multimodal, wearable patch using integrated flexible sensors advances the concept of a patched-based edge-computing system for telemedicine or telediagnosis.

ESN. Calculation of the 589.5 s datasets shown in Figure 4A takes 1.5692 and 2.2269 s using an ESN, and in the case of the 1 s dataset for real-time prediction, time delays were only 2.66 and 3.78 ms for arrhythmia and activity detections, respectively, which are negligible time costs for detections.

Figures 4H and 4I show continuous analysis results from the vital signals of arrhythmias (Figure S8) and falls (Figure 4A), respectively, using this multimodal wearable sensor patch and optimization algorithm. These data confirm that continuous datasets are well matched with human behaviors and reveal that this algorithm can be applied to a variety of subjects with relatively high accuracy without adding further training data from each user.

Smartphone app user interface

Data analysis algorithms shown in Figure 1E were installed as an app on Android smartphones. Since the app has all the developed algorithms, it does not need to use a cloud to analyze data. However, because the software differs between computers (Python) and smartphones (Dart), some programs were composed to work in real-time data analyses of vital signals. Although there is a ~ 5 s delay in displaying the analyzed results on the smartphone, it was confirmed that the output signals were the same as the output data analyzed by a more powerful computer (Figure 5; Video S1). The smartphone app stored all raw data of ECG, respiration, skin humidity, skin temperature, and activity in the smartphone as well as analyzed data using the ESN and conditional branches.

Conclusion and outlook

An edge-computing, multimodal, wearable sensor patch was developed for remote healthcare monitoring. Multiple sensors

EXPERIMENTAL PROCEDURES

Fabrication process

The multimodal, wearable sensor patch comprises four sensors to detect respiration, skin humidity, skin temperature, and ECG. First, silver

(Ag) electrodes were formed using screen printing on both sides of a PET film (Figure S1, 1). After cutting the PET with a laser (Figure S1, 2), Ag paste was applied and cured to electrically connect the top and bottom Ag electrodes formed on the PET film. Another PET film was then laminated over the Ag electrodes as a passivation and protection layer (Figure S1, 3).

For the strain sensor, first, a CO₂ laser (VLS2.30 UNIVERSAL Laser System) was used to expose a polyimide (PI) film, such that multi-layered, defected LIG was formed due to the heating of PI caused by laser exposure.¹¹ Next, a PDMS solution was spin coated over the LIG/PI. After curing the PDMS, it was delaminated from the PI film. Due to the porous nature of the LIG, it was transferred into the PDMS layer. This LIG/PDMS film was used as a strain sensor for respiration monitoring and was bonded on the PET film aligned with the Ag electrode. The surface of the PET film was treated with oxygen plasma and 3-aminopropyltriethoxysilane (APTES) to make a strong chemical bond between the PET and PDMS films (Figure S1, 4).

A temperature sensor was fabricated on a PI film. A spin-coated PI film was prepared on a handling Si wafer. SiO₂ was deposited on the PI film to enhance the adhesiveness for metal deposition. Cr/Au (thickness: 5/30 nm) was deposited with an electron beam evaporator, and a lift-off process was employed to pattern it. This metal layer was used as a temperature sensor. After delamination of the PI film with patterned metal layers, the sensor film was laminated on the PET film using double-sided tape (Figure S1, 5). To create a stable electrical connection between Ag and Cr/Au, Ag paste was applied between them when it was laminated.

For a humidity sensor, ZIS nanosheets were first synthesized from a mixture of ZnCl₂, InCl₃·4H₂O, and thioacetamide, followed by the process reported previously.^{24,27} This ZIS solution was drop cast over interdigitated LIG electrodes on a PI film and cured at 100°C for 20 min. After forming a hole in the PI film for skin humidity ventilation to the environment, the ZIS/PI film was laminated on the PET film with Ag paste and double-sided tape (Figure S1, 5). To allow for safe, reliable adhesion to skin, a medical adhesion sheet (Perme-role, Nitto Denko) was laminated on the back of the PET film (Figure S1, 6). Because the PET film, which has low water vapor transmission, was used as the main film for the patch, many small holes were formed over the entire PET film, except for the sensor region, to enhance breathability (Figure S1, 7). Finally, gel electrodes for ECG detection on the back side of the PET film, a waterproof filter (TEMISH, Nitto Denko) to prevent direct sweat contact with the humidity sensor, and a PDMS cup with an air cavity to block environmental temperature change⁷ were formed on the wearable sensor patch (Figure S1, 8). The structure of the final fabricated device is shown in Figures 2C–2E.

Data process

Data of the skin temperature sensor shown in Figures 3, S5, and S6 were processed by using a moving average of 20 s. The black line for the HR was extracted by applying a median smoothing function using the Igor Pro software, which replaced outliers in data with the median of neighboring values. The black line for respiration was calculated by using a function of percentile using the Igor Pro software. The setting of percentile function was to make the median of the values in 50 data points.

ESN

For ESNs with K inputs, N reservoir nodes, and L outputs, \mathbf{u} is the K -dimensional external input, \mathbf{x} is the L -dimensional reservoir activation function, and \mathbf{y} is the L -dimensional output. \mathbf{W}^{in} , \mathbf{W} , and \mathbf{W}^{out} are the input, internal, and output weight matrices, respectively. \mathbf{W}^{in} is uniformly distributed with $w_{ij}^{in} \in [-\sigma, \sigma]$. This σ is called “input scaling” and is a hyperparameter that determines the weights of the input layer of the reservoir. When the leaking rate is α , the ESN in this study is created as follows²⁸:

$$\mathbf{x}_{n+1} = (1 - \alpha)\mathbf{x}_n + f(\mathbf{W}^{in}[1, \mathbf{u}_n] + \mathbf{W}\mathbf{x}_n)$$

$$\mathbf{y}_{n+1} = g(\mathbf{W}^{out}, [1, \mathbf{u}_{n+1}, \mathbf{x}_{n+1}]).$$

f is a sigmoid function (we used tanh) and g is output activation function (a sigmoid or softmax functions is used in this study.). Here, the bias term is given

at the same time as the input \mathbf{u} . When obtaining the output, the direct path from the input to the output was also connected at the same time to improve accuracy. When ρ is the spectral radius of \mathbf{W} , the relationship at the condition noted below is satisfied.²⁸

$$\rho \leq \alpha$$

In this condition, a grid search was conducted for four parameters: the number of nodes in the internal layer, the spectral radius, the input scaling, and the leaking rate. Furthermore, in order to classify the status of several parameters, logistic regression from the open-source library “scikit-learn”²⁹ was used, and “max_iter” was set to 10,000 with default settings for the others.

Conditional branch for arrhythmia detection

Arrhythmia detection was conducted using two results, one of which was the ESN result and the other was the conditional branch result. Classification by a conditional branch detects ventricular extrasystolic beats. These are arrhythmias in which the ventricles are stimulated earlier than the sinus node rhythm, resulting in ventricular excitation. A typical example of a ventricular extrasystole shows a long pause after its appearance. To find this long pause symptom, the RRI of ECG signals was classified as a conditional branch.

First, Q, R, and S (QRS) waves were extracted from the ECG sensor. In the derivation of QRS waves, a sliding window of about 100 ms was prepared, and the standard deviation was obtained within that interval (Figures S19A and S19B). When the standard deviation exceeded 0.2, it was defined as a QRS wave (Figure S19C). This threshold value was determined empirically by observing the results of the ECG sensor. The widths of the two most recent QRS waves were defined as w_1 and w_2 , and the two most recent RRIs were d_1 and d_2 . The average value of the normal RRI (RRI_{ave}) was calculated using the average value of d_1 and d_2 , satisfying the following conditions.

Condition 1: $0.9 d_2 < d_1 < 1.1 d_2$ and $0.9 d_1 < d_2 < 1.1 d_1$.

Condition 2: $d_1 > 30$ steps and $d_2 > 30$ steps (30 steps corresponds to HR 250 BPM)

Condition 1 ensures that d_1 and d_2 are approximately the same length, corresponding to a normal pulse-to-pulse distance. Furthermore, since the ECG sensor detects noise caused by muscle movement generated by coughing (Figure 4D), noise is sometimes mistakenly judged as a QRS wave. For an accurate calculation of RRI_{ave} , a condition regarding the distance of the QRS waves was added (condition 2). Condition 2 omits abnormally short RRIs caused by noise. For arrhythmia detection, two more conditions were defined using RRI_{ave} below.

Condition 3: $d_2 < 1.25 \times RRI_{ave}$ and $d_1 < 0.75 \times RRI_{ave}$.

Condition 4: $w_1 < 30$ steps and $w_2 < 30$ steps (30 steps corresponds to 0.25 s).

Condition 3 confirms a pulse that occurs earlier than the rhythm of stimulation from the sinus node, which is an example of a typical ventricular extrasystolic contraction. Condition 4 is used to eliminate the abnormally wide QRS caused by muscle movement, such as coughing.

Data acquisition and processing

The sampling rates of the ECG sensor (125 Hz) and the acceleration sensor (10 Hz) used in this study are different. To input data into the ESN simultaneously, acceleration sensor data were pre-processed by up-sampling to match the ECG data (Figure S20). In addition, a constant multiplier was applied to all sensor data to be in the range of approximately –1 to 1. This pre-processing allows results to be treated equally, independent of the amplitude.

Finally, post-processing was introduced for output results in detected falls, coughing, and arrhythmias. When output results are positive, a smoothing process to keep positive output at least ~250 ms was introduced to make stable, reliable results. Because these physiological actions do not have multiple outputs at such high speed, this post-processing does not affect the reliability of the analyses. For activity detection, a sliding window of approximately 800 ms was prepared. If positive states are detected at least twice within the period, a smoothing process is introduced to continue outputting positive states from the first to the last. This contributes to reducing the number of reservoir nodes that hold the memory of the ESN and accomplishing fast calculations.

Activity detection

When creating training data in activity detection, $\delta = 0.3$ and $\delta = -0.3$ were added to data from the acceleration sensor Z as an augmentation (Figures S16C and S16D). This data processing was used to compensate for slight differences in subject posture, and empirically, a value of ± 0.3 was valid for this analysis. This augmentation improves $F_{\beta\alpha}$ from 0.815 to 0.964. A comparison of uses of ESNs and conditional branches is discussed in Note S2 and Figure S21.

Arrhythmia detection

In arrhythmia detection, training data were created from ECG sensor outputs from a subject with arrhythmia. Arrhythmia signals and arrhythmia-like noise are shown in Figures S11A and S11B, respectively. Gaussian noise with a standard deviation of 1 and a mean of 0 was added to the normal ECG waveform (Figure S11D). The addition of Gaussian noise mimicked noise generated in the ECG sensor when subjects moved. Without this data augmentation, the accuracy* was 0.086, whereas it improved to 0.286 with augmentation.

Cough detection

In cough detection, when the ECG sensor and the acceleration sensor Z were simultaneously inputted to one ESN, the best accuracy* was 0.669 (Figure S22). Here, the reservoir node was fixed at 420, which was the same as the total of two nodes when two different reservoir layers were used (Figure 1E). When the effect of a malfunction on postural changes was removed, the accuracy rate became 0.704, which is less accurate than when two reservoir layers were employed.

When subjects cough, a signal with a large amplitude from the ECG sensor output is obtained. To prevent fault detection as a cough by just checking the large amplitude signal, the ECG signal was added as an augmentation (Figure S13E). The result was 0.537 without augmentation. In Figure 4F, it can be said that each detection system is sufficiently accurate.

Edge computing in a smartphone

A UI software development kit, Flutter, was used to develop a smartphone application. The application was compiled directly in native machine code, which ensures high performance and responsiveness. We used the Dart programming language for Android in this study (Google Pixel 5a). The architecture of the application consists of BLE communication processing, RC processing, and graph display processing. To achieve real-time processing, these are processed asynchronously. In BLE communication processing, the microcontroller was designated as peripheral, and the smartphone was central in the BLE protocol. They communicate using the notify method. In the notify method, the microcontroller (peripheral) sends sensor data to the smartphone (central) as soon as the data are ready. Therefore, the smartphone is set to receive data at any time. Each data packet contains 5 acceleration datasets for the x, y, and z axes, temperature, humidity, strain, and ECG data. The application stores the data in an array. The packets are then divided to create time-series data arrays. The RC process detects several items such as activity, falls, posture changes, coughs, and arrhythmias. The system is designed to compute across multiple steps because it is necessary to use previous data or update results of past reservoir computations. Each detection process is conducted step by step as soon as data for a particular step are recorded. In the graph display process, reservoir outputs are displayed in real time on graphs for each step. Additionally, acceleration data and ECG data are displayed numerically.

Physiological experiments

Subjects attached the sensor patch to their chests. Data were transferred from the circuit to the smartphone via Bluetooth, and the results were displayed in real time on a computer or smartphone monitor. Human subject experiments were performed in compliance with a protocol approved by the ethics committee at Osaka Metropolitan University and Hokkaido University. Informed consent was obtained from all volunteers to record and use all data.

RESOURCE AVAILABILITY

Lead contact

Data that support the findings of this study are available upon reasonable request from the corresponding author and lead contact, Kuniharu Takei (takei@ist.hokudai.ac.jp).

Materials availability

The materials can be produced following the procedures described in [fabrication process](#).

Data and code availability

All data of this study are available upon reasonable request from the lead contact. The original code can be found at <https://doi.org/10.5281/zenodo.13143072>.

ACKNOWLEDGMENTS

This work was partially supported by the JST AIP Accelerated Program (no. JPMJCR21U1), JSPS KAKENHI (grant nos. JP22H00594 and JP24H00887), the Murata Science Foundation, the Hitachi Global Foundation, and the Takeda Science Foundation.

AUTHOR CONTRIBUTIONS

K.T. conceived the ideas and designed the research. G.M., S.H., Y.K., and H.N. fabricated and characterized the devices. G.M., S.W., K.N., and K.T. performed the data analysis. G.M. and K.N. developed the ESN algorithm. T.K., Y.M., H.H., and K.H. developed the smartphone app. G.M., K.H., K.N., and K.T. wrote the manuscript with input from all authors.

DECLARATION OF INTERESTS

K.T. is an inventor on a patent application about a humidity sensor in this paper.

SUPPLEMENTAL INFORMATION

Supplemental information can be found online at <https://doi.org/10.1016/j.device.2024.100597>.

Received: May 31, 2024

Revised: July 16, 2024

Accepted: September 24, 2024

Published: October 30, 2025

REFERENCES

- Mayer, C., Tyler, J., Fang, Y., Flora, C., Frank, E., Tewari, M., Choi, S.W., Sen, S., and Forger, D.B. (2022). Consumer-Grade Wearables Identify Changes in Multiple Physiological Systems During COVID-19 Disease Progression. *Cell Rep. Med.* 3, 100601. <https://doi.org/10.1016/j.xcrm.2022.100601>.
- Chung, H.U., Rwei, A.Y., Hourlier-Fargette, A., Xu, S., Lee, K., Dunne, E.C., Xie, Z., Liu, C., Carlini, A., Kim, D.H., et al. (2020). Skin-Interfaced Biosensors for Advanced Wireless Physiological Monitoring in Neonatal and Pediatric Intensive-Care Units. *Nat. Med.* 26, 418–429. <https://doi.org/10.1038/s41591-020-0792-9>.
- Takaya, M., Matsuda, R., Inamori, G., Kamoto, U., Isoda, Y., Tachibana, D., Nakamura, F., Fuchiwaki, O., Okubo, Y., and Ota, H. (2021). Transformable Electrocardiograph Using Robust Liquid-Solid Heteroconnector. *ACS Sens.* 6, 212–219. <https://doi.org/10.1021/acssensors.0c02135>.
- Yamamoto, Y., Harada, S., Yamamoto, D., Honda, W., Arie, T., Akita, S., and Takei, K. (2016). Printed Multifunctional Flexible Device with an Integrated Motion Sensor for Health Care Monitoring. *Sci. Adv.* 2, e1601473. <https://doi.org/10.1126/sciadv.1601473>.

5. Xuan, Y., Hara, H., Honda, S., Li, Y., Fujita, Y., Arie, T., Akita, S., and Takei, K. (2022). Wireless, Minimized, Stretchable, and Breathable Electrocardiogram Sensor System. *Appl. Phys. Rev.* 9, 011425. <https://doi.org/10.1063/5.0082863>.
6. Zhang, Y., Webb, R.C., Luo, H., Xue, Y., Kurniawan, J., Cho, N.H., Krishnan, S., Li, Y., Huang, Y., and Rogers, J.A. (2016). Theoretical and Experimental Studies of Epidermal Heat Flux Sensors for Measurements of Core Body Temperature. *Adv. Healthcare Mater.* 5, 119–127. <https://doi.org/10.1002/adhm.201500110>.
7. Xu, K., Lu, Y., Yamaguchi, T., Arie, T., Akita, S., and Takei, K. (2019). Highly Precise Multifunctional Thermal Management-Based Flexible Sensing Sheets. *ACS Nano* 13, 14348–14356. <https://doi.org/10.1021/acsnano.9b07805>.
8. Xie, R., Du, Q., Zou, B., Chen, Y., Zhang, K., Liu, Y., Liang, J., Zheng, B., Li, S., Zhang, W., et al. (2019). Wearable Leather-Based Electronics for Respiration Monitoring. *ACS Appl. Bio Mater.* 2, 1427–1431. <https://doi.org/10.1021/acsabm.9b00082>.
9. Zhong, J., Li, Z., Takakuwa, M., Inoue, D., Hashizume, D., Jiang, Z., Shi, Y., Ou, L., Nayem, M.O.G., Umezu, S., et al. (2022). Smart Face Mask Based on an Ultrathin Pressure Sensor for Wireless Monitoring of Breath Conditions. *Adv. Mater.* 34, e2107758. <https://doi.org/10.1002/adma.202107758>.
10. Escobedo, P., Fernández-Ramos, M.D., López-Ruiz, N., Moyano-Rodríguez, O., Martínez-Olmos, A., Pérez de Vargas-Sansalvador, I.M., Carvajal, M.A., Capitán-Vallvey, L.F., and Palma, A.J. (2022). Smart Face-mask for Wireless CO₂ Monitoring. *Nat. Commun.* 13, 72. <https://doi.org/10.1038/s41467-021-27733-3>.
11. Xu, K., Fujita, Y., Lu, Y., Honda, S., Shiomi, M., Arie, T., Akita, S., and Takei, K. (2021). A Wearable Body Condition Sensor System with Wireless Feedback Alarm Functions. *Adv. Mater.* 33, e2008701. <https://doi.org/10.1002/adma.202008701>.
12. Gao, W., Emaminejad, S., Nyein, H.Y.Y., Challa, S., Chen, K., Peck, A., Faghan, H.M., Ota, H., Shiraki, H., Kiriya, D., et al. (2016). Fully Integrated Wearable Sensor Arrays for Multiplexed *in situ* Perspiration Analysis. *Nature* 529, 509–514. <https://doi.org/10.1038/nature16521>.
13. Lin, S., Yu, W., Wang, B., Zhao, Y., En, K., Zhu, J., Cheng, X., Zhou, C., Lin, H., Wang, Z., et al. (2020). Noninvasive Wearable Electroactive Pharmaceutical Monitoring for Personalized Therapeutics. *Proc. Natl. Acad. Sci. USA* 117, 19017–19025. <https://doi.org/10.1073/pnas.2009979117>.
14. Sempionatto, J.R., Lin, M., Yin, L., De la Paz, E., Pei, K., Sonsa-Ard, T., de Loyola Silva, A.N., Khorshed, A.A., Zhang, F., Tostado, N., et al. (2021). An Epidermal Patch for the Simultaneous Monitoring of Haemodynamic and Metabolic Biomarkers. *Nat. Biomed. Eng.* 5, 737–748. <https://doi.org/10.1038/s41551-021-00685-1>.
15. Wang, B., Zhao, C., Wang, Z., Yang, K.-A., Cheng, X., Liu, W., Yu, W., Lin, S., Zhao, Y., Cheung, K.M., et al. (2022). Wearable Aptamer-Field-Effect Transistors Sensing System for Noninvasive Cortisol Monitoring. *Sci. Adv.* 8, eabk0967. <https://doi.org/10.1126/sciadv.abk0967>.
16. Min, J., Demchyshyn, S., Sempionatto, J.R., Song, Y., Hailegnaw, B., Xu, C., Yang, Y., Solomon, S., Putz, C., Lehner, L., et al. (2023). An Autonomous Wearable Biosensor Powered by a Perovskite solar Cell. *Nat. Electron.* 6, 630–641. <https://doi.org/10.1038/s41928-023-00996-y>.
17. Ye, C., Wang, M., Min, J., Tay, R.Y., Lukas, H., Sempionatto, J.R., Li, J., Xu, C., and Gao, W. (2024). A Wearable Aptamer Nanobiosensor for Non-Invasive Female Hormone Monitoring. *Nat. Nanotechnol.* 19, 330–337. <https://doi.org/10.1038/s41565-023-01513-0>.
18. Honda, S., Tanaka, R., Matsumura, G., Seimiya, N., and Takei, K. (2023). Wireless, Flexible, Ionic, Perspiration-Rate Sensor System with Long-Time and High Sweat Volume Functions Toward Early-Stage, Real-Time Detection of Dehydration. *Adv. Funct. Mater.* 33, 2306516. <https://doi.org/10.1002/adfm.202306516>.
19. Yuan, Z., Hou, L., Bariya, M., Nyein, H.Y.Y., Tai, L.C., Ji, W., Li, L., and Davey, A. (2019). A Multi-Modal Sweat Sensing Patch for Cross-Verification of Sweat Rate, Total Ionic Charge, and Na(+) Concentration. *Lab Chip* 19, 3179–3189. <https://doi.org/10.1039/c9lc00598f>.
20. Kwon, K., Kim, J.U., Deng, Y., Krishnan, S.R., Choi, J., Jang, H., Lee, K., Su, C.-J., Yoo, I., Wu, Y., et al. (2021). An On-Skin Platform for Wireless Monitoring of Flow Rate, Cumulative Loss and Temperature of Sweat in Real Time. *Nat. Electron.* 4, 302–312. <https://doi.org/10.1038/s41928-021-00556-2>.
21. Lu, Y., Fujita, Y., Honda, S., Yang, S.H., Xuan, Y., Xu, K., Arie, T., Akita, S., and Takei, K. (2021). Wireless and Flexible Skin Moisture and Temperature Sensor Sheets toward the Study of Thermoregulator Center. *Adv. Healthcare Mater.* 10, e2100103. <https://doi.org/10.1002/adhm.202100103>.
22. Nakajima, K., and Fischer, I. (2021). *Reservoir Computing: Theory, Physical Implementation, and Applications* (Springer Nature).
23. Xu, C., Solomon, S.A., and Gao, W. (2023). Artificial Intelligence-Powered Electronic Skin. *Nat. Mach. Intell.* 5, 1344–1355. <https://doi.org/10.1038/s42256-023-00760-z>.
24. Lu, Y., Xu, K., Zhang, L., Deguchi, M., Shishido, H., Arie, T., Pan, R., Hayashi, A., Shen, L., Akita, S., and Takei, K. (2020). Multimodal Plant Healthcare Flexible Sensor System. *ACS Nano* 14, 10966–10975. <https://doi.org/10.1021/acsnano.0c03757>.
25. Jaeger, H. (2001). Technical Report GMD Report. The "echo State" Approach to Analysing and Training Recurrent Neural Networks - with an Erratum Note, 148, pp. 1–47.
26. Jaeger, H. (2002). Short Term Memory in Echo State Networks. *GMD Report* 152, 1–60.
27. Honda, S., Hara, H., Arie, T., Akita, S., and Takei, K. (2022). A Wearable, Flexible Sensor for Real-Time, Home Monitoring of Sleep Apnea. *iScience* 25, 104163. <https://doi.org/10.1016/j.isci.2022.104163>.
28. Jaeger, H., Lukosevicius, M., Popovici, D., and Siewert, U. (2007). Optimization and Applications of Echo State Networks With Leaky-Integrator Neurons. *Neural Network* 20, 335–352. <https://doi.org/10.1016/j.neunet.2007.04.016>.
29. Pedregosa, F., Varoquaux, G., Gramfort, A., Michel, V., Thirion, B., Grisel, O., Blondel, M., Prettenhofer, P., Weiss, R., Dubourg, V., et al. (2011). Scikit-Learn: Machine Learning in Python. *J. Machine Learning Res.* 12, 2825–2830.